

AN ENHANCED DEEP LEARNING APPROACH FOR TECTONIC FAULT AND FRACTURE EXTRACTION IN VERY HIGH RESOLUTION OPTICAL IMAGES

Bilel Kanoun^{1,2} , Mohamed Abderrazak Cherif^{1,3} , Isabelle Manighetti¹ ,
Yuliya Tarabalka³ , Josiane Zerubia² 

¹ Université Côte d’Azur, Observatoire de la Côte d’Azur, IRD, CNRS, Géoazur, Valbonne, France

e-mail: {kanoun, mcherif, manighetti}@geoazur.unice.fr

² Inria, Université Côte d’Azur, Sophia Antipolis, France

e-mail: {bilel.kanoun, josiane.zerubia}@inria.fr

³ LuxCarta Technology, Sophia Antipolis, France

e-mail: {mcherif, ytarabalka}@luxcarta.com

ABSTRACT

Identifying and mapping fractures and faults are important in geosciences, especially in earthquake hazard and geological reservoir studies. This mapping can be done manually in optical images of the earth surface, yet it is time consuming and it requires an expertise that may not be available. Building upon a recent prior study, we develop a deep learning approach, based on a variant of a U-Net neural network, and apply it to automate fracture and fault mapping in optical images and topographic data. We show that training the model with a realistic knowledge of fracture and fault uneven distributions and trends, and using a loss function that operates at both pixel and larger scales through the combined use of weighted Binary Cross Entropy and Intersection over Union, greatly improves the predictions, both qualitatively and quantitatively. As we apply the model to a site differing from those used for training, we demonstrate its enhanced generalization capacity.

Index Terms— Image processing, Curvilinear feature extraction, Deep convolutional neural network, VHR optical imagery, Tectonic faults and fractures.

1. INTRODUCTION

Fractures and faults are ubiquitous on earth and contribute to a number of important processes: small-scale fractures (i.e., length $< 10^2$ m) control the permeability of rock reservoirs [1]; larger-scale faults (i.e., length $> 10^3$ m) may produce damaging earthquakes [2]; faults and fractures combine to weaken the rocks or materials they affect [3]; etc. To better understand earthquakes, fluid pathways, rock strength, etc., it is thus necessary to identify fracture and fault networks in the material or region of concern. One approach is to search for the traces these fractures and faults may form at the ground surface, in the exposed rocks. The mapping of these traces

allows recovering the architecture of the fault and fracture networks [4, 5]. This architecture, which generally reveals to be dense and complex [6], in turn provides clues to understand the fault and fracture mechanics and the mechanical behavior of the fractured or faulted material [7–9].

So far, mapping fractures and faults at the ground surface has been done manually, based on the visual detection of their traces in field outcrops or in remote optical images of the earth surface [9, 10]. However, this visual detection and manual mapping of the fault traces is labor-intensive and requires an expertise that is not always available. In particular, while fractures have generally simple, short, linear traces, faults have longer (up to $10^2\text{--}10^3$ km) and more complex curvilinear traces, that can be segmented laterally and inter-connected with more minor fault lines (e.g. [3, 5, 11]).

In the last decade, the progress of deep learning for the detection of curvilinear structure networks has increased, with specific developments dedicated to recover blood vessel networks in biomedical imagery [12–14]. Several deep learning techniques have also been successfully developed for the delineation of road networks [15–17]. More recently, attempts have been made to adapt these prior techniques to the detection of fractures and faults in optical remote images and topographic data [18]. In [18], Mattéo et al. proposed an upgraded version of a U-Net model, based on an architecture developed by [19]. The model revealed successful to identify and map fractures and faults with high accuracy in high resolution optical images, in regions similar to those used for training. By contrast, the predictions were fairly weak in regions with different characteristics (different rocks, fault sizes, fault topographic imprints, image texture, etc.). Using the same dataset as in [18], Jafrasteh et al. [20] have developed a Generative Adversarial Network (GAN) model to automate fractures and faults mapping. The approach succeeded to predict small fractures, but was less efficient to recognize major faults [20].

Our objective is to go a step forward and to produce a

deep learning model that can identify and map fractures and faults with high accuracy and a greater generalization capacity than in [18] and [20]. We build upon the model proposed in [18]. Since this model is not freely accessible, we first had to rebuild it using the indications provided in [18], namely a variant of the U-Net architecture with an increased number of blocks, a larger number of convolutional layers per block and the addition of skip connections. However, as the biases and weights are not provided in [18], our final model is not strictly similar (see below). We have then performed two major additions to our model, to increase its performance. The results are positive, as shown in this paper.

2. DATA

We use the same training data as in [18], but then make the predictions on a test site that was not used for training nor analyzed in [18]. This allows testing the generalization capacity of our model.

The training and test data sets are photogrammetric optical ortho-images and topographic data acquired in the Granite Dells region in Arizona, USA. The site is a large granite rock outcrop, mainly free of vegetation and anthropogenic features, and dissected by a dense network of 10^{-3} - 10^3 m long fractures and faults forming fairly clear traces at the ground surface (e.g. [6]) (Fig. 1 a-b). The ortho-image and topographic data have an ultra-high resolution pixel size of 3 mm (more details in [18]).

The training was done in two close sub-sites of the imaged zone, referred to as sites A and B in [18]. These sites are 10-15 m long and a few meters wide, so that fractures and fault traces have lengths in range 10^{-3} -10 m. The ground truth is a basic manual mapping of the fracture and fault traces done by a student with limited expertise in fault mapping. In this basic mapping, most fracture and fault traces are thus simplified while some of the actual faults and fractures were not mapped. Furthermore, all fracture and fault traces are represented with the same level of confidence, which is unlikely. Finally, the proportion of fractures and faults in the training sites is fairly low, with a much larger fraction of the sites showing no fault. The basic ground truth is thus imperfect (i.e., large uncertainties at the pixel scale), incomplete, too highly confident, and unbalanced.

The test zone (6 m wide, 20 m long; Fig. 1 a) is 2 km away from the training sites, and was not used for training nor analyzed in [18]. While fracture and fault traces have similar geomorphic signatures and lengths than in the training sites, the texture of the image is slightly different from that in the training sites. In this test zone, we have an expert manual mapping (Fig. 1 b). In this refined mapping, the fracture and fault traces were mapped more precisely than in the basic mapping, while the mapping is more exhaustive. Also, the fracture and fault traces are represented with two levels of confidence, “certain” and “uncertain” fractures and faults;

the latter includes traces whose interpretation is uncertain or having imprecise contours. Furthermore, major and more minor fractures/faults are discriminated. Although the refined ground truth is of higher accuracy than the basic ground truth, it is still imperfect (i.e., uncertainties at the pixel scale), incomplete (exhaustive manual mapping cannot be done), and unbalanced (total area with no fracture/fault is larger than total fracture/fault area).

3. METHODOLOGY

We have built a CNN architecture of U-Net type inspired from the work of [18], based on the architecture developed by [19]. We call this reference model “Tasar-Mattéo MRef” or TM-MRef. As we said earlier, we had to rebuild the model as it was not freely available. We call our new model “Bilel Kannoùn MRef” or BK-MRef. As TM-MRef, it was designed with a binary approach (i.e., a pixel is a fault or is not a fault), with the same loss function (weighted Binary Cross Entropy or wBCE), and with the same training data and procedure as described in [18]: use of 4-bands RGBT (red, green, blue + topography) and basic ground truth in sites A and B; ground truth fault lines represented with Gaussian thickness to take their location uncertainty into account; split of tiles into 2565 training sets and 375 validation samples, with the size of each tile 256×256 pixels; data augmentation including random rotations of 180° , mirror effects around x and y axis, random contrast and brightness changes, and addition of Gaussian noise (see [18]).

The predictions of the models TM-MRef and BK-MRef in the test zone are shown in Fig. 1 c-d. Both fail to predict many of the fractures and faults identified in the refined mapping. To improve the performance of BK-MRef, we thus include two major additions. Firstly, we build upon the observation that fractures and faults in the training zones have different orientations (see Fig. 3 in [18]), mainly about North-South, East-West, and NorthEast-SouthWest (apparent orientations as sites are not geo-referenced), and the fraction of fractures and faults showing one or other of these overall orientations is variable. We assume that a training that would respect the actual balance in fault trends would be more efficient. We thus used a balanced tile partition technique to train the model with tiles including similar fractions of fractures and faults having a given overall orientation. We call this training a “balanced training”. Secondly, we test different loss functions. As mentioned above, the reference models TM-MRef and BK-MRef use the wBCE given by the formula [21]:

$$\mathcal{L} = -y \times \log(\hat{y}) - \beta(1-y) \times \log(1-\hat{y}) \quad (1)$$

where y represents a pixel in the ground truth, \hat{y} is the prediction for each pixel and β is made to indicate the balance between the fault and not-a-fault classes (defined as the % of fault pixels in the ground truth).

The wBCE is well adapted to binary classifications as in our case, yet operates at the pixel scale which may be an issue when working with a ground truth with large uncertainties at the pixel level, and in a site where the two classes are unbalanced. These limitations may explain why the predictions of TM-MRef and BK-MRef are not very good (Fig. 1 c-d).

Thus, we use another loss function that better deals with imbalanced classes and uncertain ground truth: the focal loss [22]. The focal loss is a variant of the wBCE and is made to target the less represented features in the ground truth, thus here, the fractures and faults. To do that, the focal loss function "down-weights" the most represented features (not-a-fault pixels) to focus on the less represented but most meaningful features, here the fracture/fault pixels. It is written as:

$$\mathcal{L}' = -\alpha y(1 - \hat{y})^\gamma \log(\hat{y}) - (1 - y)\hat{y}^\gamma \log(1 - \hat{y}) \quad (2)$$

where α and γ are made to balance the fault and not-a-fault classes.

However, the focal loss function still operates at the pixel level, while, due to large uncertainties in the ground truth, a spatial metric taking into account the actual uncertainties on the fault locations would be more appropriate. To reach this objective, we use the Intersection over Union (IoU, or Jaccard) loss function [23] which measures the ratio between the summed number of pixels (expressed as an area) whose prediction is consistent with the ground truth, and the total area encompassing both the ground truth and the predictions. More, in order to penalize different aspects of the errors, we combine the IoU –which quantifies the overall spatial error, with the wBCE –which quantifies the pixel error.

The proposed combined loss \mathcal{L}'' is written as:

$$\mathcal{L}'' = IoU_{loss} + \mathcal{L} \quad (3)$$

$$\text{where } IoU_{loss} = J(y, \hat{y}) = 1 - \frac{y \cap \hat{y}}{y \cup \hat{y}}$$

4. EXPERIMENTAL RESULTS

During the calculations, the weights and biases given by the filters are randomly initialized respecting the theory of Glorot et al. [24]. In addition, these weights and biases are updated at each iteration during the training process using an Adam optimizer [25] characterized by a learning rate $lr=10^{-4}$, $\beta_1=0.9$ and $\beta_2=0.999$. No regularization including dropouts and batch normalization, was performed during this process. The program was coded in Python environment using the Keras deep learning library [26], on an AMD Ryzen Threadripper 1950X 16-Core 3.40-GHz processor with Linux Debian as the operating system. The GPU used was a GeForce RTX 2080 Ti work station characterized by 11 GB of memory and 3584 CUDA Cores version 11.0.

Using the same training data as in [18], we calculated five models: a first one trained as in [18] (unbalanced training) and using a wBCE loss function, called BK-MRef (Fig. 1 d); two other models testing the impact of a balanced training, with a wBCE (Fig. 1 e) or a focal loss (Fig. 1 f) function; and two other models testing the impact of the combined \mathcal{L}'' loss function, with unbalanced (Fig. 1 g) or balanced (Fig. 1 h) training. The predictions of TM-MRef are not good, as many fractures and faults fail to be predicted (Fig. 1 c). The predictions of our original reference model BK-MRef are slightly better in that they include more fractures and faults (Fig. 1 d). However, those lack along-strike continuity and many are still missing. The balanced training much improves the predictions, even with the wBCE loss function (Fig. 1 e). They are fairly noisy however, and distortions at the top and bottom boundaries of the image are mistakenly predicted as faults. When using together a balanced training and a focal loss function (Fig. 1 f), major faults become well predicted, and the distortions discriminated. However, most minor fractures/faults fail to be detected. Using the \mathcal{L}'' combined loss function greatly improves the predictions, whether a non-balanced (Fig. 1 g) or a balanced training (Fig. 1 h) is done. However, with unbalanced training, the predictions are noisy and many minor fractures and faults are represented with high probabilities, which is unrealistic. Distortions are also mistakenly predicted as faults. The predictions are much better when the model uses both a balanced training and the combined loss function \mathcal{L}'' (Fig. 1 h). Even though a few distortions are still mistakenly represented as faults, all major fractures and faults are well predicted, while minor features are also found and generally assigned lower, thus more realistic probabilities.

To assess the results more quantitatively, we use the same numerical indicators as in [18]: the Tversky similarity index (TI) [27] that evaluates the similarity between the ground truth and the prediction pixels, and the Receiver Operator Characteristic curve (ROC) [28] that compares the "False Positive Rate" to the "True Positive Rate".

We do not refer to other common metrics due to the imbalance between fault and not-a-fault classes in our dataset. Moreover, these metrics are appropriate for binary probabilities, not for probabilities spanning a broad range between 0 and 1 as it is the case here.

The TI scores (calculated for certain faults only) confirm the positive impacts of both the balance training (Table 1, lines 3-4) and the combined \mathcal{L}'' loss function (Table 1, lines 5-6). The model using both balanced data and combined loss function gives better quantitative results.

Fig. 2 shows the ROC representations for the six models. It confirms that including either balanced training or a combined loss function improves the model performance, with greater improvement achieved when balanced training and combined loss are used together.

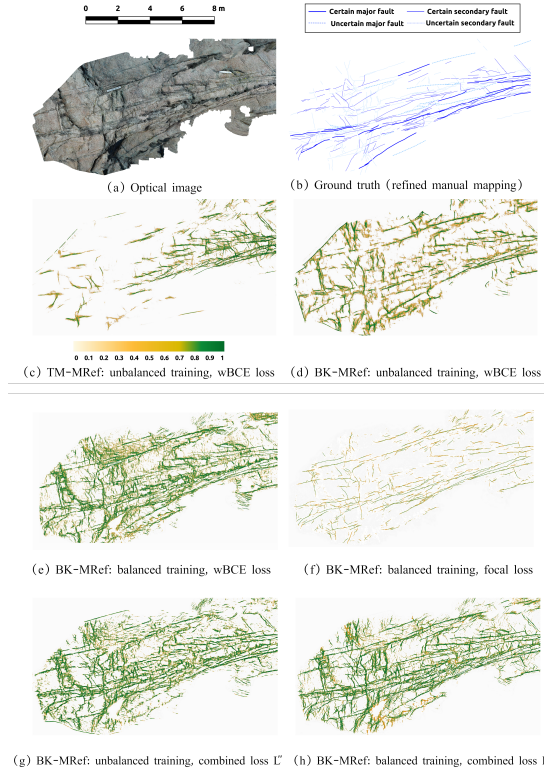


Fig. 1. Predictions in the test zone with the different approaches. (a) Optical ortho-image of the test zone. The data is not geo-referenced thus the orientation is arbitrary; (b) Manual expert mapping of fracture and fault traces (refined mapping). Different line thicknesses discriminate major and more minor faults. However we do not use this classification here. (c) Predictions using model of [18], TM-MRef, that uses unbalanced training and a wbCE loss function, (d) Predictions using our model built and trained as in [18] (unbalanced training and wbCE loss function), called BK-MRef, (e) Predictions using our model BK-MRef with a wbCE loss function, yet trained with “balanced training”, (f) Predictions using our model BK-MRef yet with a focal loss function and a “balanced training”, (g) Predictions using our model BK-MRef trained as in [18] (unbalanced training) yet with the loss function \mathcal{L}'' combining IoU and wbCE; and (h) Predictions using our model BK-MRef yet with the loss function \mathcal{L}'' combining IoU and wbCE, and a “balanced training”.

Table 1. Tversky Index (TI) calculated for the six models with respect to refined mapping

	TI
TM-MRef (unbalanced training, wbCE loss)	0.29
BK-MRef (unbalanced training, wbCE loss)	0.29
BK-MRef (balanced training, wbCE loss)	0.4
BK-MRef (balanced training, focal loss)	0.3
BK-MRef (unbalanced training, combined loss \mathcal{L}'')	0.42
BK-MRef (balanced training, combined loss \mathcal{L}'')	0.44

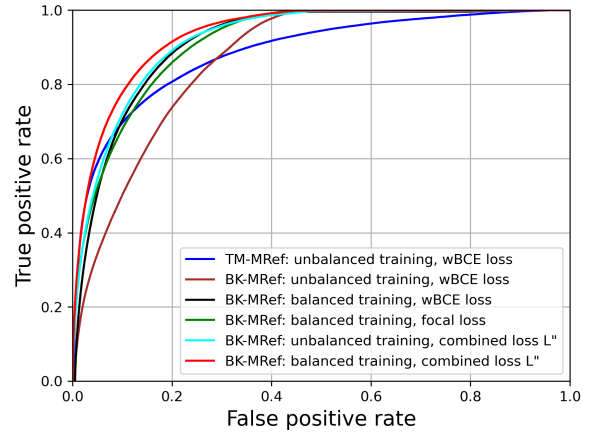


Fig. 2. ROC representations for the six models, with respect to refined mapping.

5. CONCLUSIONS

We propose an enhanced deep learning approach for faults and fractures prediction in high resolution optical and topographic data, building upon the prior works of [18] and [19]. As the ground truth is imperfect and incomplete by essence (exhaustive fault mapping cannot be done even by the best expert and cannot be accurate at the pixel scale), we had to improve the prior approaches. We show here that training the model with a realistic knowledge of the fracture and fault uneven distributions and trends improves the predictions. The choice of the loss function is even more important as the predictions need to be examined both at a pixel and a larger spatial scales. We have thus proposed a new loss function combining these two scales through the combined use of wbCE and IoU. The results are greatly improved, as demonstrated both qualitatively and quantitatively. This is especially interesting as we applied the model to a site with different characteristics than those of the zones used for training. This shows an increased generalization capacity of our model. Further work remains to be done however, in particular to test the generalization power of the model on different datasets, and to take into account the major and minor, and the certain and uncertain fault classes that we have ignored here. We expect that this will result in a fairly generic model that we will make freely available to assist geologists and geophysicists to identify fractures and faults in earth images and materials.

6. ACKNOWLEDGEMENTS

This project has been funded by the French National Research Agency (ANR Grant FAULTS_R_GEMS #ANR-17-CE31-0008), the UCA^{JEDI}. Investments in the Future project managed by the French National Research Agency (grant ANR-15-IDEX-01, Academy of excellence #3), and the French CNRS (program Imag’In).

7. REFERENCES

- [1] E. Bonnet, O. Bour, N. E. Odling, P. Davy, I. Main, P. Cowie, and B. Berkowitz, “Scaling of fracture systems in geological media,” *Reviews of geophysics*, vol. 39, no. 3, pp. 347–383, 2001.
- [2] C. H. Scholz, *The mechanics of earthquakes and faulting*, Cambridge university press, 2019.
- [3] C. Perrin, I. Manighetti, J.P. Ampuero, F. Cappa, and Y. Gaudemer, “Location of largest earthquake slip and fast rupture controlled by along-strike change in fault structural maturity due to fault growth,” *Journal of Geophysical Research: Solid Earth*, vol. 121, no. 5, pp. 3666–3685, 2016.
- [4] I. Manighetti, P. Tapponnier, P.Y. Gillot, E. Jacques, V. Courtillot, R. Armijo, J.C. Ruegg, and G. King, “Propagation of rifting along the arabia-somalia plate boundary: Into afar,” *Journal of Geophysical Research: Solid Earth*, vol. 103, no. B3, pp. 4947–4974, 1998.
- [5] C. Perrin, I. Manighetti, and Y. Gaudemer, “Off-fault tip splay networks: A genetic and generic property of faults indicative of their long-term propagation,” *Comptes Rendus Geoscience*, vol. 348, no. 1, pp. 52–60, 2016.
- [6] G. De Joussineau and A. Aydin, “The evolution of the damage zone with fault growth in sandstone and its multiscale characteristics,” *Journal of Geophysical Research: Solid Earth*, vol. 112, no. B12, 2007.
- [7] Y. Ben-Zion and C. G. Sammis, “Characterization of fault zones,” *Pure and Applied Geophysics*, vol. 160, no. 3, pp. 677–715, 2003.
- [8] I. Manighetti, G. King, and C. G. Sammis, “The role of off-fault damage in the evolution of normal faults,” *Earth and Planetary Science Letters*, vol. 217, no. 3-4, pp. 399–408, 2004.
- [9] I. Manighetti, C. Perrin, Y. Gaudemer, S. Dominguez, N. Stewart, J. Malavieille, and S. Garambois, “Repeated giant earthquakes on the wairarapa fault, new zealand, revealed by lidar-based paleoseismology,” *Scientific reports*, vol. 10, no. 1, pp. 1–11, 2020.
- [10] I. Manighetti, P. Tapponnier, V. Courtillot, Y. Gallet, E. Jacques, and P.Y. Gillot, “Strain transfer between disconnected, propagating rifts in Afar,” *Journal of Geophysical Research: Solid Earth*, vol. 106, no. B7, pp. 13613–13665, 2001.
- [11] I. Manighetti, C. Caulet, L. De Barros, C. Perrin, F. Cappa, and Y. Gaudemer, “Generic along-strike segmentation of a far normal faults, East Africa: Implications on fault growth and stress heterogeneity on seismogenic fault planes,” *Geochemistry, Geophysics, Geosystems*, vol. 16, no. 2, pp. 443–467, 2015.
- [12] O. Ronneberger, P. Fischer, and T. Brox, “U-net: Convolutional networks for biomedical image segmentation,” in *International Conference on Medical Image Computing and Computer-Assisted Intervention*. Springer, 2015, pp. 234–241.
- [13] K. Maninis, J. Pont-Tuset, P. Arbeláez, and L. Van Gool, “Deep Retinal Image Understanding,” in *International Conference on Medical Image Computing and Computer-Assisted Intervention*. Springer, 2016, pp. 140–148.
- [14] J. Son, S. J. Park, and K. H. Jung, “Towards accurate segmentation of retinal vessels and the optic disc in fundoscopic images with generative adversarial networks,” *Journal of Digital Imaging*, vol. 32, no. 3, pp. 499–512, 2019.
- [15] G. Cheng, Y. Wang, S. Xu, H. Wang, S. Xiang, and C. Pan, “Automatic road detection and centerline extraction via cascaded end-to-end convolutional neural network,” *IEEE Transactions on Geoscience and Remote Sensing*, vol. 55, no. 6, pp. 3322–3337, 2017.
- [16] A. Mosinska, M. Koziński, and P. Fua, “Joint segmentation and path classification of curvilinear structures,” *IEEE Transactions on Pattern Analysis and Machine Intelligence*, vol. 42, no. 6, pp. 1515–1521, 2019.
- [17] L. Caltagirone, S. Scheidegger, L. Svensson, and M. Wahde, “Fast LIDAR-based road detection using fully convolutional neural networks,” in *2017 IEEE Intelligent Vehicles Symposium (IV)*. IEEE, 2017, pp. 1019–1024.
- [18] L. Mattéo, I. Manighetti, Y. Tarabalka, J. Gaucel, M. Van Den Ende, A. Mercier, O. Tasar, N. Girard, F. Leclerc, T. Giampetro, S. Dominguez, and J. Malavieille, “Automatic fault mapping in remote optical images and topographic data with deep learning,” *Journal of Geophysical Research: Solid Earth*, Online: <https://doi.org/10.1029/2020JB021269>, 2021.
- [19] O. Tasar, Y. Tarabalka, and P. Alliez, “Incremental learning for semantic segmentation of large-scale remote sensing data,” *IEEE Journal of Selected Topics in Applied Earth Observations and Remote Sensing*, vol. 12, no. 9, pp. 3524–3537, 2019.
- [20] B. Jafrasteh, I. Manighetti, and J. Zerubia, “Generative adversarial networks as a novel approach for tectonic fault and fracture extraction in high resolution satellite and airborne optical images,” *ISPRS-International Archives of the Photogrammetry, Remote Sensing and Spatial Information Sciences*, vol. 43, pp. 1219–1227, 2020.
- [21] Y. Ho and S. Wookey, “The real-world-weight cross-entropy loss function: Modeling the costs of mislabeling,” *IEEE Access*, vol. 8, pp. 4806–4813, 2019.
- [22] T.Y. Lin, P. Goyal, R. Girshick, K. He, and P. Dollár, “Focal loss for dense object detection,” in *IEEE International Conference on Computer Vision*, 2017, pp. 2980–2988.
- [23] P. Jaccard, “The distribution of the flora in the alpine zone. 1,” *New Phytologist*, vol. 11, no. 2, pp. 37–50, 1912.
- [24] X. Glorot and Y. Bengio, “Understanding the difficulty of training deep feed-forward neural networks,” in *Proceedings of the thirteenth International Conference on Artificial Intelligence and Statistics*. JMLR Workshop and Conference Proceedings, 2010, pp. 249–256.
- [25] D. P. Kingma and J. Ba, “Adam: A method for stochastic optimization,” *arXiv preprint arXiv:1412.6980*, 2014.
- [26] J. Brownlee, *Deep learning with Python: develop deep learning models on Theano and TensorFlow using Keras*, Machine Learning Mastery, 2016.
- [27] A. Tversky, “Features of similarity.,” *Psychological Review*, vol. 84, no. 4, pp. 327, 1977.
- [28] K. Hajian-Tilaki, “Receiver Operating Characteristic (ROC) curve analysis for medical diagnostic test evaluation,” *Caspian Journal of Internal Medicine*, vol. 4, no. 2, pp. 627, 2013.